INTERNATIONAL JOURNAL FOR NUMERICAL METHODS IN FLUIDS
Int. J. Numer. Meth. Fluids 2004; **46**:109–125 (DOI: 10.1002/fld.746)

Assessment of volume of fluid and immersed boundary methods for droplet computations

Daniel Lörstad[1,*,†], Marianne Francois[2,‡,§], Wei Shyy[2,¶] and Laszlo Fuchs[1,‖]

[1]*Department of Heat and Power Engineering, Division of Fluid Mechanics, University of Lund, Lund, SE-22100, Sweden*
[2]*Department of Mechanical and Aerospace Engineering, University of Florida, Gainesville, FL 32611-6250, U.S.A.*

SUMMARY

The volume of fluid (VOF) and immersed boundary (IB) methods are two popular computational techniques for multi-fluid dynamics. To help shed light on the performance of both techniques, we present accuracy assessment, which includes interfacial geometry, detailed and global fluid flow characteristics, and computational robustness. The investigation includes the simulations of a droplet under static equilibrium as a limiting test case and a droplet rising due to gravity for $Re \leqslant 1000$. Surface tension force models are key issues in both VOF and IB and alternative treatments are examined resulting in improved solution accuracy. A refined curvature model for VOF is also presented. With the newly developed interfacial treatments incorporated, both IB and VOF perform comparably well for the droplet dynamics under different flow parameters and fluid properties. Copyright © 2004 John Wiley & Sons, Ltd.

KEY WORDS: interfacial flow; surface tension; volume of fluid; immersed boundary; VOF; IB

1. INTRODUCTION

Multiphase flows with droplets and bubbles are frequently encountered in nature, science and engineering. They are not easily accurately simulated due to the fact that they involve interfaces with unknown and time varying shapes that separate mass and property changes. These fluid flow problems can be modelled by treating each phase separately by either recognizing the interface as a sharp discontinuity or a smeared transition region. Depending on the particular approaches the challenges with such separated phase transport are as follows:

*Correspondence to: D. Lörstad, Department of Heat & Power Engineering, Box 118, SE-22100 Lund, Sweden.
†E-mail: Daniel.Lorstad@vok.lth.se
‡E-mail: mmfran@lanl.gov
§Present address: Los Alamos National Laboratory, MS B296, Los Alamos, NM 87545, U.S.A.
¶E-mail: wss@mae.ufl.edu
‖E-mail: Laszlo.Fuchs@vok.lth.se

Contract/grant sponsor: ELFORSK
Contract/grant sponsor: NASA URETI Program

Published online 24 June 2004

Received 10 April 2003
Revised 5 April 2004

1. Mass conservation within an individual and overall domain.
2. Numerical instabilities and wiggles caused by the property and flux discontinuities at the interface.
3. Errors associated with calculating the curvature of the droplet/bubble shape.
4. Rather simple 2D (planar or axisymmetric) models for phase transport may become very complicated in 3D.
5. Convergence problems for high density (viscosity) ratio or large surface tension.
6. Tracking change in interface topology (break-up and coalescence).
7. Difficulty in achieving more than first order accuracy when there is a lack of alignment between the grid and the interface.

Examples of different separated flow methods (review in References [1, 2]) are volume of fluid (VOF), immersed boundary (IB), sharp interface technique [3], level set [4, 5], moving-grid methods [6] and lattice Boltzmann methods [7]. Here VOF [8, 9] and IB [10, 11] are investigated and compared. They are chosen because they are popular and quite simple methods, but no detailed comparison can be found in existing literature.

VOF is based on volume averaging of the phases and the volume fraction is treated as a single field, which is advected in an Eulerian way. The advantages with VOF are that bubble break-up and coalescence are included implicitly and that VOF methods are rather easily extendable to three dimensions. The main drawback is the difficulty of calculating the interface curvature.

IB using front tracking algorithms requires the storage of additional information, namely, the interface location. The interface is advected in a Lagrangian way; therefore the main advantage with IB is that the interface is well defined and tracked in time. The main drawback is that special algorithms have to be developed in order to handle coalescence and break-up.

In this work, effort is made to clarify the various interfacial characteristics and numerical accuracy between methods and to offer guidance for future development. The main focus is on the surface tension modelling and the implications of a moving object interacting with the surrounding fluid. To facilitate the investigation, test problems including the simulations of a droplet under static equilibrium and a droplet rising due to gravity for $Re \leqslant 1000$ are adopted for detailed comparative assessment.

2. COMPUTATIONAL TECHNIQUES

2.1. Governing equations

The governing equations of mass and momentum for an unsteady, viscous, incompressible Newtonian flow may be expressed as

$$u_{j,j} = 0 \tag{1}$$

$$\rho(u_{i,t} + V_{i,t} + u_j u_{i,j}) = -p_{,i} + \{\mu(u_{i,j} + u_{j,i})\}_{,j} + \rho g_i + \sigma\kappa\delta n_i \tag{2}$$

where u_i is the velocity, V_i is the grid velocity, p is the pressure, ρ is the local fluid density, μ is the local dynamic viscosity, g_i is the gravitational acceleration, σ is the surface tension

Table I. Summary of methods.

Method	VOF	IB
Two-phase flow method	Eulerian method	Mixed Eulerian–Lagrangian
Equation formulation	3D	Axisymmetric
Single phase flow solver	Simultaneous p-U update	Projection method
Multigrid	Multigrid for p and u	Multigrid for p
Interface tracking	Phase function α	Marker points
Surface tension models	VOF1, VOF2	IB1, IB2
Normal and curvature	Computed based on α	Based on marker points
Second phase transport	Eulerian transport using Youngs's model	Advection of the Lagrangian particles
Time marching	Explicit for α, fully implicit for other variables	Explicit
Smoothing length γ where h is the cell width	$3h$ $(h = h_x = h_y = h_z)$	$2h$ $(h = h_r = h_z)$

coefficient, κ is the curvature of the interface, n_i is the interface unit normal and δ is Dirac's distribution function, which is zero everywhere except at the interface. For VOF, the Equations (1) and (2) are applied on a 3D (x, y, z) co-ordinate system whereas for IB the conservative formulations of (1) and (2) are applied on a 2D axisymmetric (r, z) co-ordinate system.

2.2. Numerical techniques for VOF model

The governing Equations (1) and (2) are discretized on a Cartesian staggered grid using second order central differences for all spatial derivatives except for the convective terms where a first order upwind scheme is applied. The accuracy of the spatial discretizations of the momentum equations is improved to third order for convective terms and fourth order for other terms by a single-step defect correction [12, 13]. The reason for using defect correction instead of a pure high order scheme is related to the enhanced stability properties of the low order algorithm combined with the accuracy of the high order operator. The transient terms are discretized using a second order accurate fully implicit temporal scheme. The pressure–velocity coupling is done through a simultaneous update of the dependent variables, similar to the one for single-phase flow used by Fuchs and Zhao [14], but modified in order to include two phases. A multigrid method is used in order to improve the convergence rate [14]. The VOF model is summarized in Table I.

2.3. VOF and phase transport

Volume of fluid (VOF) is a widely used approach for bubble and droplet transport [15–20]. VOF is based on phase averaging where the VOF phase indicator variable α defines the quantity of each fluid in each computational cell.

The phase field α is tracked using the transport equation:

$$\alpha_{,t} + (u_j \alpha)_{,j} = 0 \tag{3}$$

which is solved by the use of a 3D direction split Youngs's method [8, 9] based on the 2D Eulerian scheme described by Rudman [21]. In the direction split method, one time step of

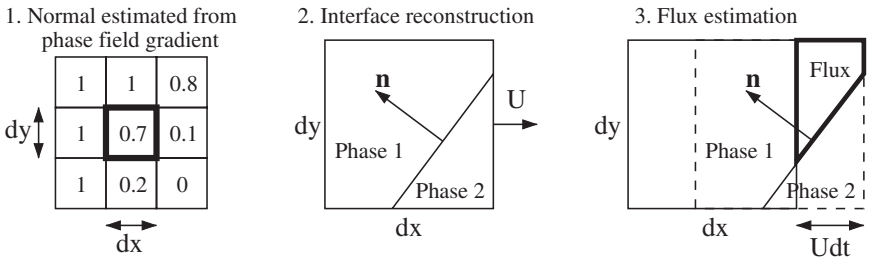

Figure 1. A three-step example in 2D of Eulerian phase transport using Youngs's method.

the 3D problem is solved using three 1D problems solved one after the other, one in each direction. In order to avoid systematic errors, the order of the directions is interchanged each time step.

In order to estimate the outgoing fluxes of α for each cell, Youngs's method is used [22]. It is chosen for its ability to keep the interface sharp as regular advection schemes rapidly smear the interface over several cells. Youngs's method is based on a geometrical strategy as opposed to finite-difference discretizations. For each cell, the normal vector of the interface and the volume fraction are used to reconstruct the interface by the use of a plane, which divides the cell into two parts (see Figure 1). This reconstruction is then used to determine the fluxes out of the cell as the plane is moved in the outflow direction.

Since the velocity update is implicit in time and the phase transport scheme is explicit, the phase transport is updated N times for each implicit time step using an N times smaller time step. In this study $N \leqslant 5$ is used.

2.4. Numerical techniques for IB model

The numerical technique employed is based on the mixed Eulerian–Lagrangian method of Shyy *et al.* [1] and Udaykumar *et al.* [23], where the above conservation equations are solved on a fixed Cartesian mesh, and the interface is represented by a set of discrete points advected in a Lagrangian way. The present IB technique is summarized in Table I and is presented in detail along with benchmark cases in Francois [10] and in Francois and Shyy [11].

The projection method or fractional-step method originally formulated by Chorin [24] is employed in order to solve the coupled mass and momentum equations. Specifically, the second-order accurate, two-step fractional step method presented in Ye *et al.* [25] is used to solve the flow equations. The mass and momentum equations are discretized using a finite-volume formulation on a fixed Cartesian mesh using a cell-centred collocated arrangement for all the variables. In order to ensure mass conservation, a face-cell velocity variable is introduced for computing the volume flux. The convection terms are discretized with a second order accurate Adams–Bashforth scheme and the diffusion terms with a second order Crank–Nicolson scheme. To speed up the computation, a multigrid technique is employed to solve the pressure equation.

2.5. IB and interface tracking

The interface discontinuity is treated by the immersed boundary method introduced by Peskin [26]. In this approach the interface is considered to be of small non-zero thickness within which the fluid properties change smoothly.

The interface is represented by K marker points of co-ordinates $\mathbf{x}_k$ with $k = 1, 2, \ldots, K$. The markers are uniformly distributed along the interface. Since the location of the Lagrangian interface points does not coincide with the fixed Eulerian grid points, the velocity field stored at the cell-centre of each grid is interpolated in order to obtain the velocity of the interface points. At each time step, the interface position is advected in a Lagrangian way and the total mass of the droplet is enforced within specified criteria (here taken as 0.01%) [27, 28].

2.6. Fluid property modelling for VOF and IB

The fluid properties can be calculated using the phase field distribution and for VOF the density is obtained using a smoothed phase variable field $G(\alpha)$:

$$\rho = \rho_1 + (\rho_2 - \rho_1)G(\alpha) \tag{4}$$

where $G(\alpha)$ is a weight defined by

$$G(\alpha(\mathbf{x}_{ijk})) = \frac{\sum_{l,m,n} \alpha_{lmn} K(|\mathbf{x}_{ijk} - \mathbf{x}_{lmn}|, \gamma)\, \mathrm{d}x\, \mathrm{d}y\, \mathrm{d}z}{\sum_{l,m,n} K(|\mathbf{x}_{ijk} - \mathbf{x}_{lmn}|, \gamma)\, \mathrm{d}x\, \mathrm{d}y\, \mathrm{d}z} \tag{5}$$

where the summation are taken over the entire domain and $K(r, \gamma)$ is taken to be [19]

$$K(r,\gamma) = \begin{cases} \gamma^3 - 6\gamma r^2 + 6r^3 & \text{if } r < \gamma/2 \\ 2(\gamma - r)^3 & \text{if } \gamma/2 < r < \gamma \\ 0 & \text{otherwise} \end{cases} \tag{6}$$

where the indices ijk and lmn refer to the cell number in the x, y and z directions, where r is the distance between x_{lmn} and x_{ijk} and where γ is the smoothing length-scale (see Table I).

For IB, with the interface location known with respect to the grid, the material properties are assigned in each fluid using the same linear dependence as in Equation (4) but based on a smooth discrete Heaviside step function $H(\xi)$ instead of $G(\alpha)$. Here $H(\xi)$ is defined as

$$H(\xi) = \begin{cases} 0 & \text{if } \xi \leqslant -\gamma \\ 1 & \text{if } \xi \geqslant +\gamma \\ \prod_{m=1}^{\dim} \frac{1}{2}\left(1 + \frac{\xi_m}{\gamma} + \frac{1}{\pi}\sin\frac{\pi\xi_m}{\gamma}\right) & \text{otherwise} \end{cases} \tag{7}$$

where $\xi = \mathbf{x} - \mathbf{x}_k$, dim is the space dimension, γ is the transition distance (see Table I), $\mathbf{x}$ is the grid co-ordinate and $\mathbf{x}_k$ is the interfacial marker co-ordinate.

The viscosity can be calculated using the corresponding linear dependence on the phase variables $G(\alpha)$ or $H(\xi)$, respectively. The smoothing length-scale γ in Table I for VOF and IB are chosen in order to attain the accuracy for each method and for various test cases as presented in References [8–10].

2.7. Surface tension modelling for VOF and IB

The surface tension forces may be modelled using the continuum surface force model (CSF) introduced by Brackbill *et al.* [29]. For VOF, the last term of Equation (2) is replaced by

$$\delta \cdot n_i = \alpha_{,i} \tag{8}$$

In order to estimate the curvature $\kappa = -\nabla \cdot \mathbf{n}$ different approaches have been used. The first VOF model (VOF1) uses a 3D variant of the 2D curvature estimation described by Rudman [19] where the interface normal is given by $\mathbf{n} = \nabla G/|\nabla G|$. Thus, the curvature can be expressed as

$$\kappa = -\frac{G_{,ii}}{(G_{,i}G_{,i})^{1/2}} + \frac{G_{,i}G_{,j}G_{,ij}}{(G_{,i}G_{,i})^{3/2}} \tag{9}$$

VOF1 has a clear drawback since neither finite-difference discretizations of a discontinuous variable nor a smoothed variable (where interface information is lost) yields high accuracy.

More appropriate for a discontinuous field is direction averaged curvature models (DAC), which is used in VOF2. DAC estimates the interface location using space averaging of the phase field in a specified direction and then the curvature can be calculated in a similar way as for marker point methods. The space averaging is done using the α field by estimating the mean value of the interface location in each cell columns in the direction of the largest normal component $n_{\max}$, as shown in Figure 2 where $n_z = n_{\max}$. All cells that are required for the interface estimation are found by the use of a plane, which approximates the interface. The normal can then be defined by

$$\mathbf{n} = \begin{pmatrix} n_x \\ n_y \\ n_z \end{pmatrix} = \frac{\alpha_{,z}}{|\alpha_{,z}|} \cdot \begin{pmatrix} -F_{,x} \\ -F_{,y} \\ 1 \end{pmatrix} \tag{10}$$

where F is the interface estimation in $n_{\max}$-direction, shown in Figure 2, where $|\partial F/\partial x| \leqslant 1$ and $|\partial F/\partial y| \leqslant 1$ since the z-direction is in the direction of the largest normal component.

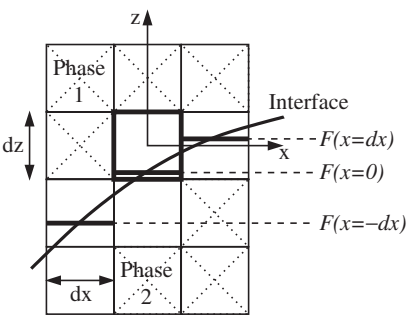

Description of VOF2

1. Find the direction of the largest normal component (z–direction in this example)
2. Estimate the interface by a plane
3. Obtain the cell averaged interface location in z–direction: F(–dx), F(0), F(dx) using the cells in the close region of the plane
4. Determine the curvature

Figure 2. A 2D example of an interface and how the curvature is estimated using VOF2.

The curvature is calculated in all cells that contain the interface using

$$\kappa = \frac{n_z}{|n_z|}\left(\frac{F_{,ii}}{|\mathbf{n}|} - \frac{F_{,i}F_{,j}F_{,ij}}{|\mathbf{n}|^3}\right) \tag{11}$$

where $F = F(x, y)$ and hence the problem is reduced from $\kappa = f(\alpha(x, y, z))$ to $\kappa = f(F(x, y))$. If $n_{\max} = n_x$ or $n_{\max} = n_y$ then the corresponding expressions for the curvature are $\kappa = f(F(y,z))$ or $\kappa = f(F(x,z))$, respectively. A smoothing function similar to Equation (5) is used when distributing the calculated curvature values to all cell edges, which have a non-zero gradient of α (Equation (8)). Compared to the curvature model by Renardy and Renardy [20], no time-consuming minimization procedure is needed here.

For IB, the curvature estimation is straightforward. The interface is parameterized as a function of the arc length s by fitting quadratic polynomials through three consecutive marker points. Once the interface position is known, the normal vector and the curvature are evaluated at the marker position by taking the appropriate derivatives of the piecewise polynomials

$$\mathbf{n} = \left(-\frac{r_s}{\sqrt{z_s^2 + r_s^2}}, \frac{z_s}{\sqrt{z_s^2 + r_s^2}}\right) \tag{12}$$

$$\kappa = \frac{z_s}{r(z_s^2 + r_s^2)^{3/2}} + \frac{r_s z_{ss} - r_{ss} z_s}{(z_s^2 + r_s^2)^{3/2}} \tag{13}$$

The distribution of the surface forces can be applied in different ways and here two different schemes are investigated. The first model, IB1, spreads the interface forces acting on the marker points to the nearby grid points via a discrete Delta function. The forces are evaluated as

$$\sigma\kappa\delta\mathbf{n} = \oint_C \sigma\kappa_k \mathbf{n}_k \delta(\xi)\,\mathrm{d}s \tag{14}$$

where C is the interface contour, s is the arc length and δ is the 'Dirac' delta function, which is taken to be

$$\delta(\xi) = \begin{cases} \prod_{m=1}^{\dim} \frac{1}{2\gamma}\left(1 + \cos\frac{\pi\xi_m}{\gamma}\right) & \text{if } |\xi| \leqslant \gamma \\ 0 & \text{otherwise} \end{cases} \tag{15}$$

In the second model, IB2, the surface tension forces are distributed in a similar way as VOF (Equation (8)) but where α is replaced by $H(\xi)$ (Equation (7)). The curvature values on grid positions (κ_{ij}) are interpolated using $\delta(\xi)$ from the curvature values at marker positions (κ_k).

3. RESULTS AND DISCUSSION

3.1. Initial mass of a droplet

The first study involves an investigation of the error in total mass of a liquid sphere for both VOF and IB. Figure 3 (left) shows the error in mass versus grid size where D is the diameter

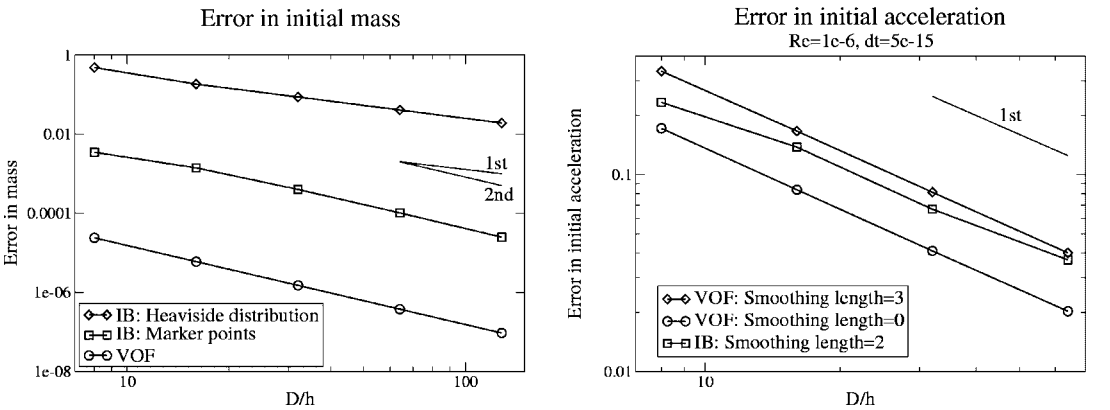

Figure 3. Error in initial mass (left) and initial acceleration (right) for a sphere versus grid size.

of the liquid sphere, h is the cell width and the error is defined as $|m_{\text{initial}} - m_{\text{analytical}}|/m_{\text{analytical}}$. The error in initial mass for VOF is very small since the initial estimation of α in each cell is made using finer cells of size $h_{\text{fine}} = h/2^6$. For IB, the error in initial mass shows a second order accurate behaviour when integrated using the marker points, but the accuracy is reduced to first order when the error is calculated from the smooth discrete Heaviside distribution of Equation (7). This shows the importance of proper distribution schemes for IB if a density field more than first order accurate is to be obtained.

3.2. Initial acceleration

The second investigation involves the transient behaviour of a fixed liquid sphere of density and viscosity equal to the outside fluid. The sphere is initially at rest and is subject to a body force (b_z) causing a flow through it. Phase change is not considered in this problem. Although this test case has no physical meaning, it is a good numerical test. The analytical initial acceleration should equal the body force, i.e. $a_{\text{analytical}}(t=0) = b_z$. Figure 3 (right) shows the error of the initial acceleration of the flow inside the sphere as a function of cell size for a small time step. The error is defined as $|a_{\text{initial}} - b_z|/b_z$. The smoothing length γ is defined according to Table I and in addition $\gamma = 0$ is used for VOF. The accuracy of the acceleration shows a first order accurate behaviour in both time and space. Note that the smoothing of the phase field strongly affects the accuracy of the initial acceleration as shown in Figure 3 with respect to body forces (such as gravity), whereas the differences between the methods seem small.

3.3. Static droplet

A common problem for multiphase flows is the surface tension modelling. Since the surface tension forces are proportional to the curvature, which is in turn proportional to the second derivatives of the interface location, surface force modelling is sensitive to errors in the interface prediction. Therefore, the CSF model has difficulties when simulating flows where the interfacial forces are dominating. Then the numerical (unphysical) fluxes normal to the

surface dominate, which result in a less accurate solution. An appropriate test case for the spurious currents is the simulation of a droplet without gravity with a zero velocity field as the initial condition [20, 30–32].

In order to eliminate any error due to spurious currents, the distribution of the surface tension forces should be made in a consistent manner that satisfies equilibrium between surface tension forces and pressure gradients without disturbing the flow field. For VOF the momentum equations (Equation (2)) for a zero velocity field are reduced to

$$p_{,i} = \sigma\kappa\alpha_{,i} \tag{16}$$

which for constant surface tension coefficient and curvature result in

$$p = \sigma\kappa\alpha \tag{17}$$

Hence the surface tension forces should be proportional to the gradient of α, where the same discretization scheme has to be applied for both α and pressure gradients. The same conclusion was also drawn by Renardy and Renardy [20]. For IB the α field is replaced by the smooth discrete Heaviside function.

Renardy and Renardy [20] have significantly reduced the problem of spurious currents but the problem is far from 'eliminated' as they claim. They only investigated their model with high viscous fluids of equal density. Further investigations are needed regarding fluids of low viscosity, since the max velocity of the spurious currents is roughly proportional to σ/μ [30], as well as fluids of high-density ratio.

Here, comparison is made to the studies of Renardy and Renardy [20] (Case 1) and Williams *et al.* [31] (Case 2). The test cases consist of a cubic domain (cylinder for IB) with sides of two diameters where a spherical droplet is placed in the middle. For Case 1 [20], the following parameters are used: $D = 0.25,\ \sigma = 0.357,\ \rho_o = \rho_d = 4,\ \mu_o = \mu_d = 1,\ \Delta t = 0.0001$ and $N_{\Delta t} = 20$. The indices o and d refer to the outer fluid and droplet fluid respectively, Δt is the time step length and $N_{\Delta t}$ is the number of time steps. Case 2 [31] is inviscid and uses: $D = 4,\ \sigma = 73,\ \rho_o = 0.1,\ \rho_d = 1,\ \mu_o = \mu_d = 0,\ \Delta t = 0.001$ and $N_{\Delta t} = 50$.

In order to focus on the behaviour of the surface tension treatment, the same discretization schemes are used for VOF and IB for these test cases. Therefore, in this section, the defect correction for VOF is not applied and IB uses first order upwind scheme for the convection terms. For this specific test case, with the analytical solution of a zero velocity field, one can express the velocity as $u \sim h^n$ where n is the order of accuracy of the problem, which yields the convection terms proportional to $u \cdot \Delta u/h \sim h^{2n-1}$. Thus, if $n > 1$ the convection terms will vanish faster than other errors as the grid is refined and the order of accuracy of the convection terms does not affect the order of accuracy of the problem.

A first test is to specify the curvature and the initial pressure field as the analytical values. The resulting errors in maximum velocity and pressure are of the order of round off ($\sim 10^{-12}$) for both VOF and IB2, whereas for IB1 the results are similar with estimated and analytical curvature. Meier *et al.* [32] have also performed this test (specifying the analytical curvature) and found only a small improvement. The present results obtained with both VOF and IB2 confirm that the curvature estimation is the only source of error when the surface tension forces are distributed in a consistent way with the flow equations. This is in agreement with Renardy and Renardy [20].

Figures 4 and 5 show the results of the investigation when using estimated curvature. The figures show the maximum error in the curvature and the maximum error in velocity versus

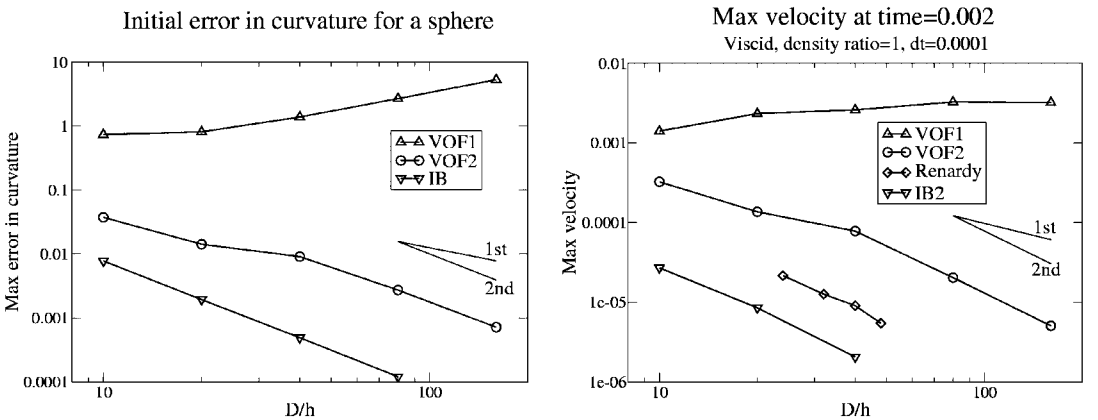

Figure 4. Max error in initial curvature (left) and max error in velocity for Case 1 (right) versus grid size for a droplet under static equilibrium.

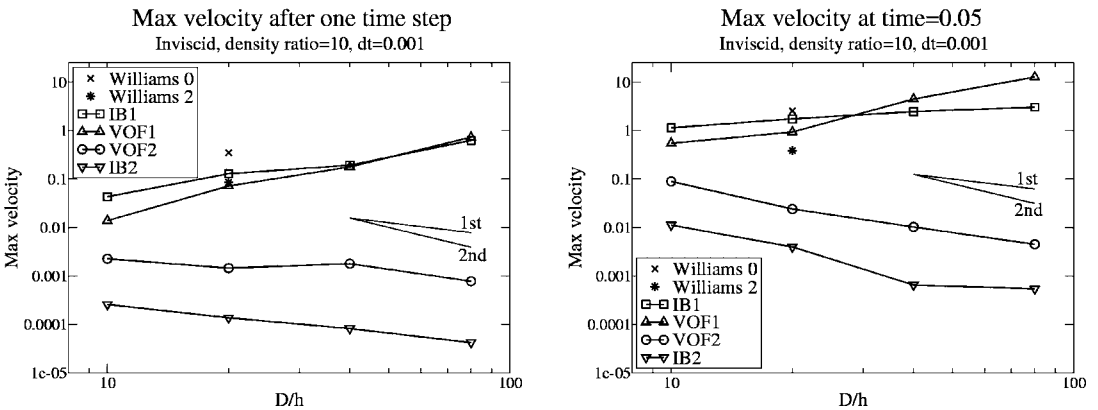

Figure 5. Max error in velocity for Case 2 after one time step (left) and after 50 time steps (right) for a droplet under static equilibrium.

D/h after a certain number of time steps, in order to compare with the results of Renardy and Renardy [20] and Williams *et al.* [31].

The maximum error of the initial curvature is shown in Figure 4 (left), which demonstrates that VOF1 does not converge with grid refinement. VOF2 indicates a similar second order accurate behaviour as IB, even though its error level is an order of magnitude higher. For VOF the curvature is estimated in all cells where $0<\alpha<1$.

In order to investigate the effect of curvature estimation on the flow field, the error in velocity is also studied. The maximum velocity for Case 1 in Figure 4 (right) shows a consistent second order accurate trend as for the curvature. Note that the maximum velocity is equal to the maximum error since the analytical solution is a zero velocity field. The error level of the parabolic interface reconstruction VOF model of Renardy and Renardy [20] is around one order less than for VOF2 but not as low as IB2.

Figure 5 shows the maximum velocity for Case 2, both after one time step and after 50. The maximum velocity after one time step is one order less than that for the initial curvature as shown in Figure 4 (left). This results in a first order error in maximum velocity for IB2 and VOF2, whereas the results for the other models do not converge, as the grid is refined. The reduced order of accuracy for Case 2 compared to Case 1 is due to a discontinuous density field. After 50 time steps ($t = 0.05$ units) the error level is higher but the basic trends are the same. VOF1 and IB1 seem to achieve comparable accuracy as the results reported by Williams *et al.* [29], whereas VOF2 and IB2 are significantly better.

The results show the need for investigation of the grid dependence when studying surface tension models. The lack of convergence as the grid is refined for VOF1 is due to the curvature estimation and the reason can be explained by studying a flat surface which is not aligned with the grid. In contrast to VOF1, both IB and VOF2 reproduce the analytical curvature value of zero for any flat surface. The curvature for VOF1 can be rewritten as $\kappa = f(G)/h$ according to Equation (9), where G is obtained by smoothing of the α field (Equations (5)–(6)). The smoothing results in a small max-error ε in the G-field where ε reduces with increased γ but not with reduced h (for a plane). Therefore, if $\gamma \sim h$ then $f(G)$ is of the same order of magnitude for all h and the error in curvature is $\sim 1/h$.

Even though the error in curvature is a lot larger for VOF1 compared with IB1, the maximum velocity is of the same order of magnitude for both cases. This stresses the importance of appropriate force distribution. It is worthwhile noting that the errors for static droplet simulations are mainly related to the error in curvature for VOF and IB2. For IB2 the initial error in curvature is only related to the distance between the marker points. This yields the possibility of high accurate results on coarse cell sizes when using fine marker point distribution. For VOF a finer grid for α than for other variables may be used as described by Rudman [19].

3.4. Rising droplet at modest Reynolds number

In order to evaluate the alternative implementations of both VOF and IB while solving the complete set of the Navier–Stokes equations, the next test case involves a droplet in a liquid rising due to gravity. A modest Reynolds number of 10 is used in order to make the flow field accurately resolved without requiring very large number of grid points. In addition, a sensitivity study of the surface tension force models is conducted. Table II shows the dimensionless numbers that define the different test cases, where the indices 1 and 2 refer to the outer and inner fluid, respectively. The variables are made non-dimensional by using the characteristic length (D is the initial diameter of the droplet), the characteristic velocity ($U = (g \cdot D)^{1/2}$ where g is gravity) and the characteristic time scale ($\tau = D/U$).

Table II. Cases for rising droplet at low *Re*.

Case	Dens. ratio	Visc. ratio	*Re*	*Fr*	*We*	*Eo*
Definition	ρ_1/ρ_2	μ_1/μ_2	$\rho_1 UD/\mu_1$	$U/(gD)^{0.5}$	$\rho_1 U^2 D/\sigma$	$\Delta\rho D^2 g/\sigma$
A	2	1	10	1	∞	∞
B	2	1	10	1	40	20

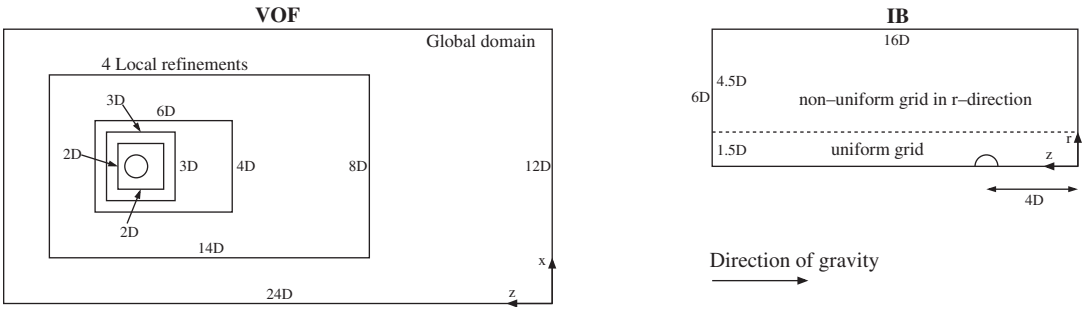

Figure 6. Grids for VOF (left) and IB (right), which are used for the simulations of the droplet rising due to gravity.

Table III. Comparison of efficiency for the simulation of a rising droplet at low *Re* until $t = 10$.

Method	D/h	Number of cells	Conver. Criteria	Time step size	Simulation time	Time per cell	Time per cell and time step
VOF	64	3.9×10^6	10^{-4}	0.005	≈ 5 days	0.11 s	5.5×10^{-5} s
IB	64	8.1×10^4	10^{-3}	0.001	3–4 h	0.15 s	1.6×10^{-5} s

The VOF simulations are performed using a uniformly moving reference frame following the droplet and a time step of $dt = 0.32h/D$ where h is the cell width in the region close to the droplet. The computational domain is $(12D, 12D, 24D)$ in direction (x, y, z), respectively where z is the gravity direction. The droplet is placed at $(x, y, z) = (6, 6, 18.25)$. Four levels of local refinements, which result in 16 times smaller cells in each direction, are used to increase the grid resolution around the droplet as shown in Figure 6.

The IB simulations are performed using a fixed reference frame and a constant time step of 0.001. The computational domain in direction (r, z) is $(6D, 16D)$ and the droplet is initially placed at $(r, z) = (0, 4)$, see Figure 6. The mesh is uniform near the droplet $(r < 3R)$ but the cell size in r-direction increases away from the droplet.

Both methods use no-slip condition on the walls and, according to Harmaty [33], this yields a wall effect of around 0.7% on the terminal velocity when compared with an infinite large domain. The simulations last until time equals 10 non-dimensional units. An efficiency comparison of VOF and IB is shown in Table III when using a single processor (Alpha 850 MHz). The results show that IB is 3–4 times faster than VOF when comparing the total simulation time per number of cells and time steps (last row in Table III) which is reasonable due to the fact that VOF uses 3D cells, implicit scheme for the velocities and slightly finer convergence criteria (final residual relative initial residual). However, the implicit velocity scheme allows for larger time step sizes and therefore VOF is slightly faster when comparing the total simulation time per number of cells. The total losses of α (or volume) in the VOF simulations relative to the initial distribution are less than 10^{-7} and for IB the loss in mass is restricted using the mass conservation criteria for the IB method (see Section 2.5).

The time dependent solutions for the rise velocity and the aspect ratio are shown in Figure 7, using VOF2 and IB2 and with a grid resolution of $D/h = 64$. The differences between VOF

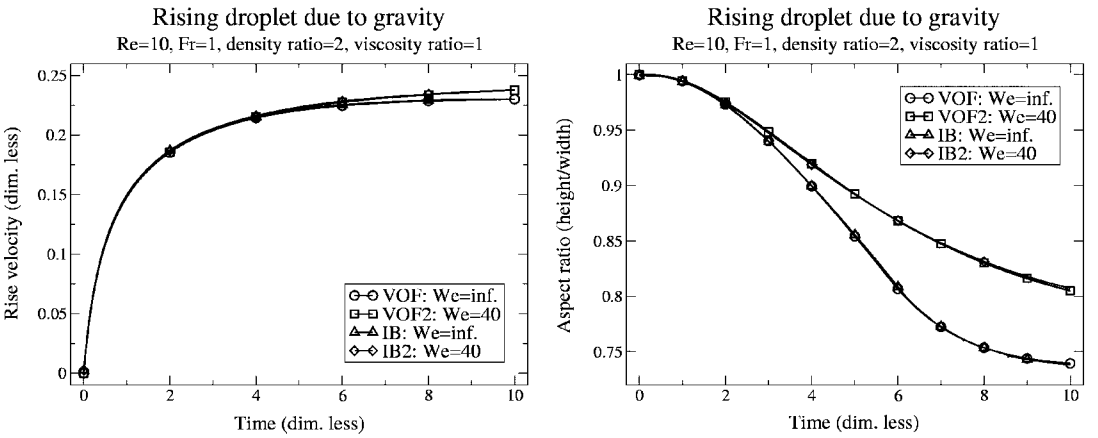

Figure 7. Rise velocity (left) and aspect ratio (right) versus time for grid size $D/h = 64$ for a rising droplet at low *Re*.

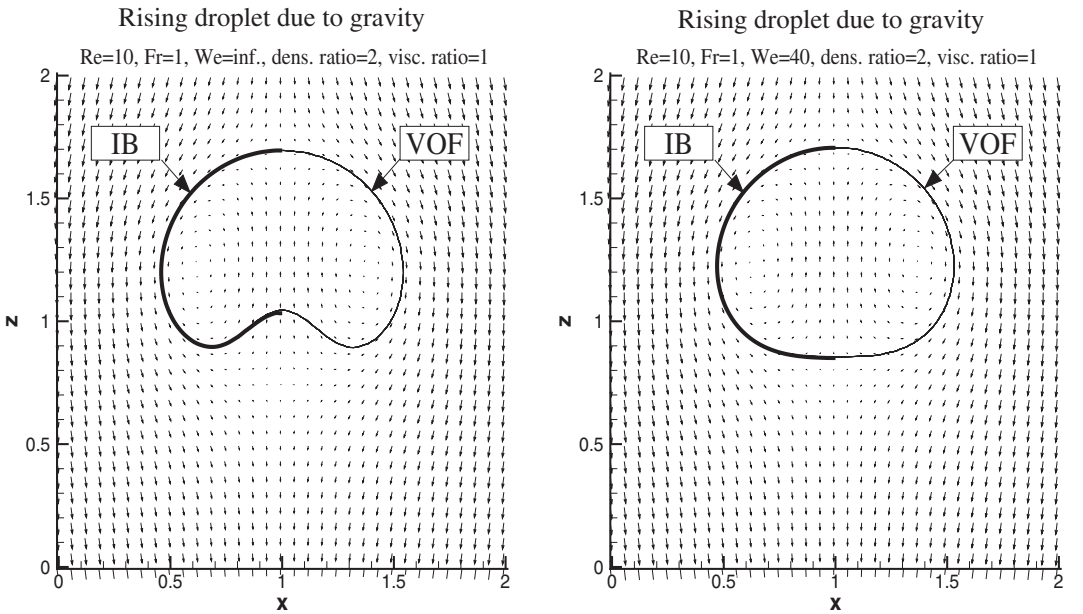

Figure 8. Rising droplet at low *Re* at $t = 10$ for $We = \infty$ (Case A, left) and $We = 40$ (Case B, right) for grid size $D/h = 64$.

and IB are small. The velocity of the droplet is defined by $\Sigma[(1-\alpha)U_z]/\Sigma(1-\alpha)$ where $\alpha = 0$ defines the droplet region. The aspect ratio is defined as the ratio between the maximum distances between the interfaces in the flow direction (z) and the orthogonal direction (x, y or r). The flow fields at the middle section using VOF2 are shown in Figure 8 at $t = 10$ for Cases A and B using a reference frame following the droplet. The droplet shape is added into

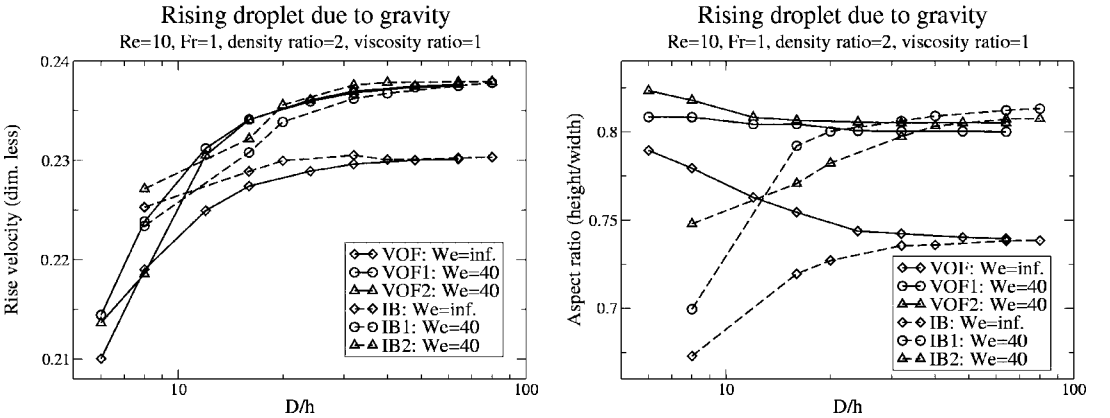

Figure 9. Rise velocity (left) and aspect ratio (right) versus grid size at $t = 10$ for a rising droplet at low *Re*.

the figures and the thin shape lines represent the contour of $\alpha = 0.5$ from VOF2 and the thick lines represent the marker point distribution from IB2. Clearly the shapes that are obtained using the different methods are similar.

The grid dependency test is shown for the same variables at $t = 10$ in Figure 9. It seems that at least 24 cells per initial diameter are required to attain adequate numerical accuracy. Furthermore, both VOF and IB under-predict the velocity on coarse grids, whereas the aspect ratio is over-predicted for VOF and under-predicted for IB.

For Case B ($We = 40$ in Figure 9), the difference between VOF2 and IB2 for $D/h = 64$ is very small for both velocity and aspect ratio and the main part of the remaining difference is probably due to the different domain sizes adopted. On the other hand, both VOF1 and IB1 perform poorly even on the finer grids. They converge to different values of aspect ratio compared with VOF2 and IB2, as the grid is refined. This phenomenon is consistent with that observed for the static droplet.

Even though the terminal velocity U_T is not obtained here, the results for Case B can be compared to the diagram of Clift *et al.* [34] where $U_T \approx 0.3$, which shows qualitative agreement. Furthermore, the terminal velocity is $U_T \approx 0.26$ for a viscous drop with a drag coefficient of $C_D = C_D^{stokes}(1 + 0.15 \times Re^{0.687})$ where $C_D^{stokes} = 20/Re$ due to the viscosity ratio of unity [34].

3.5. *Rising droplet at high Reynolds number*

The last test case involves a higher Reynolds number in order to investigate the behaviour of VOF2 and IB2 for more convectively dominated conditions. Case B of Table II but with a *Re* of 1000 is chosen for the study. This type of droplet is expected to wobble and perhaps also break-up but here the focus is on the initial stage of the droplet rise and the first velocity peak. Comparison of wobbling behaviour using axisymmetric and 3D simulations is an interesting topic but that is out of the scope of this work.

Figure 10 shows the velocity development and aspect ratio versus time, respectively, with $D/h = 64$. Figure 11 shows the velocity field at $t = 2.5$ using VOF2 and the shapes using VOF2

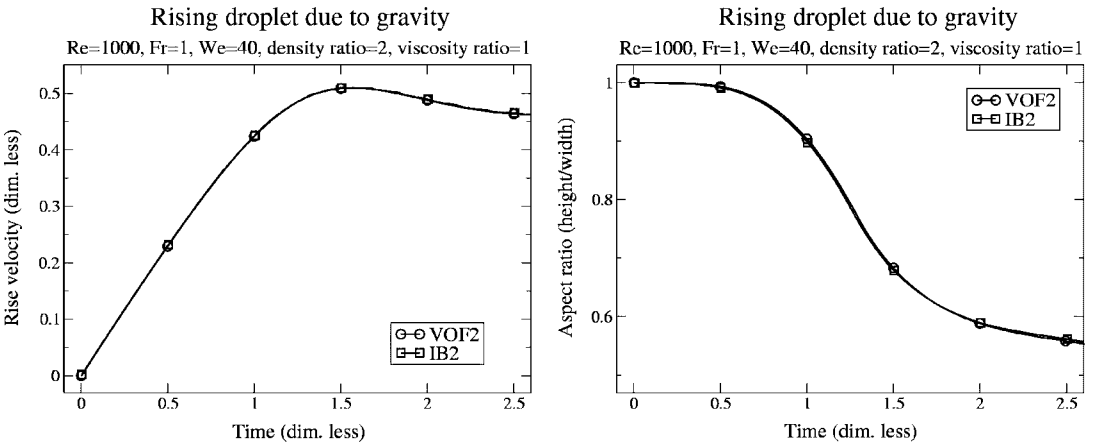

Figure 10. Rise velocity (left) and aspect ratio (right) versus time for grid size $D/h = 64$ for a rising droplet at high Re.

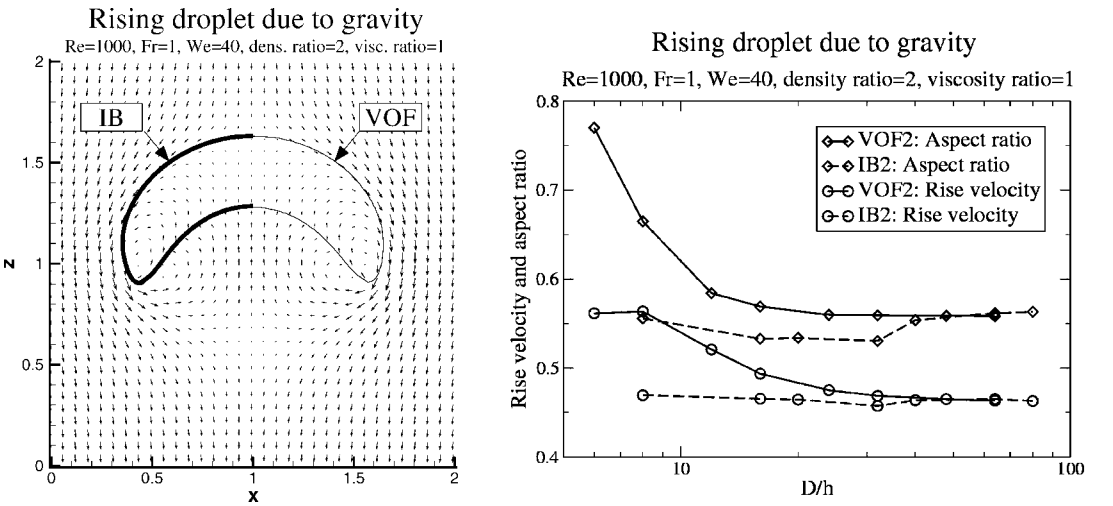

Figure 11. Rising droplet at high Re at $t = 2.5$ for $We = 40$ and grid size $D/h = 64$. Left: shape and flow field. Right: rise velocity (left) and aspect ratio (right) versus grid size.

(thin line: contour of $\alpha = 0.5$) and IB2 (thick line: marker point distribution). Figure 11 also shows the grid refinement effect for $t = 2.5$. The error on coarse grids is much larger for VOF2 than for IB2 but as the grid is refined the results between VOF2 and IB2 converge to the same value. Furthermore, the mass loss is similar to that of the low Re droplets.

4. CONCLUDING REMARKS

The methods of volume of fluid (VOF) and immersed boundary (IB) are evaluated and compared.

First, assessment is made for errors related to conserving initial mass after defining the droplet interface. VOF can handle this aspect in a more straightforward way in comparison with IB since the volume of each phase is directly assigned. Here, a spatial accuracy of second order is used for VOF. For IB, the error is first order in space when the mass is computed using the smooth discrete Heaviside distribution and second order when computed from the marker points.

For the test case of a droplet under static equilibrium, the investigations also include different surface tension models. It is shown that the accuracy is greatly improved when the surface tension forces are distributed in a consistent way with the discretization of the flow equations (IB2), compared to a previously developed scheme (IB1). The curvature estimation is important for the accuracy and that usually is a challenging topic for VOF. However, the newly proposed curvature model (VOF2) shows similar high accuracy as IB2, even though the level of the error in general is an order of magnitude higher. VOF2 and IB2 show second order accurate behaviour in space for the first set of fluid properties but the accuracy is reduced to first order for the second test case where the density ratio differs from unity and the flow is inviscid. VOF1 and IB1 are not converging for either case as the grid is refined.

The simulations of a droplet rising due to gravity at modest Re indicated that the results agree well between VOF and IB for the case of no surface tension forces ($We = \infty$) and for VOF2 and IB2 for the case with surface tension forces ($We = 40$). However, the droplet aspect ratios differ for VOF1 and IB1. This indicates further the improved accuracy of VOF2 and IB2. The agreement between the results for VOF2 and IB2 is also shown to hold for higher Re.

ACKNOWLEDGEMENTS

This work was a part of the Swedish research program Vattenturbinteknik in collaboration with the University of Florida. The Department of Heat and Power Engineering, University of Lund, was financially supported by ELFORSK and the Swedish National Energy Administration and the Department of Mechanical and Aerospace Engineering, University of Florida, by the NASA URETI program. This support is highly appreciated.

REFERENCES

1. Shyy W, Francois M, Udaykumar HS, N'Dri N, Tran-Son-Tay R. Moving boundaries in micro-scale biofluid dynamics. *Applied Mechanics Reviews* 2001; **54**:5.
2. Shyy W, Udaykumar HS, Rao MM, Smith RW. *Computational Fluid Dynamics with Moving Boundaries*. Taylor and Francis: London, 1996.
3. Ye T, Shyy W, Chung JC. A fixed-grid, sharp-interface method for bubble dynamics and phase change. *Journal of Computational Physics* 2001; **174**:781–815.
4. Sethian JA. *Level Set Methods and Fast Marching Methods*; *Evolving Interfaces in Computational Geometry*, *Fluid Mechanics*, *Computer Vision*, *and Material Science* (2nd edn). Cambridge University Press: Cambridge, 1999.
5. Stanley JO, Ronald PF. *Level Set Methods and Dynamic Implicit Surfaces*. Springer: Berlin, 2002.
6. Takagi S, Matsumoto Y, Huang H. Numerical analysis of a single rising bubble using boundary-fitted coordinate system. *JSME International Journal Series B* 1997; **40**(1):42–50.

7. Watanabe T, Ebihara K. Numerical simulation of coalescence and breakup of rising droplets. *Computers and Fluids* 2003; **32**:823–834.
8. Lörstad D. Numerical modelling of deforming bubble transport related to cavitating hydraulic turbines. *Ph.D. Dissertation*, University of Lund, Sweden, September 2003. Free download at: http://www.fm.vok.lth.se/.
9. Lörstad D, Fuchs L. High order surface tension VOF-model for 3D bubble flows with high density ratio. *Journal of Computational Physics* (in press).
10. Francois M. Computations of drop dynamics with heat transfer. *Ph.D. Dissertation*, University of Florida, USA, August 2002. Free download at http://www.uflib.ufl.edu/etd.html.
11. Francois M, Shyy W. Computations of drop dynamics with the immersed boundary method, Part 1: numerical algorithm and buoyancy-induced effect. *Numerical Heat Transfer Part B* 2003; **44**:101–118.
12. Fuchs L. Defect-corrections and higher numerical accuracy. In *Proceedings of the GAMM-Seminar on* '*Efficient Solutions of Elliptic Systems*', Hackbusch W (ed.). Kiel: 1984; 52–66.
13. Gullbrandt J, Bai XS, Fuchs L. High order Cartesian grid method for calculation of incompressible turbulent flow. *International Journal for Numerical Methods in Fluids* 2001; **36**:687–709.
14. Fuchs L, Zhao H-S. Solution of three-dimensional viscous incompressible flows by a multi-grid method. *International Journal for Numerical Methods in Fluids* 1984; **4**:539–555.
15. Bussmann M, Mostaghimi J, Chandra S. On a three-dimensional volume tracking model of droplet impact. *Physics of Fluids* 1999; **11**(6):1406–1417.
16. Chen L, Garimella SV, Reizes JA, Leonardi E. The development of a bubble rising in a viscous liquid. *Journal of Fluid Mechanics* 1996; **387**:61–96.
17. Gueyffier D, Li J, Nadim A, Scardovelli R, Zaleski S. Volume-of-Fluid interface tracking with smoothed surface stress methods for three-dimensional flows. *Journal of Computational Physics* 1999; **152**:423–456.
18. Puckett EG, Almgren AS, Bell JB, Marcus DL, Rider WJ. A high-order projection method for tracking fluid interfaces in variable density incompressible flows. *Journal of Computational Physics* 1997; **130**:269–282.
19. Rudman M. A volume-tracking method for incompressible multifluid flows with large density variations. *International Journal for Numerical Methods in Fluids* 1998; **28**:357–378.
20. Renardy Y, Renardy M. PROST: A parabolic reconstruction of surface tension for the Volume of Fluid method. *Journal of Computational Physics* 2002; **183**:400–421.
21. Rudman M. Volume-tracking methods for interfacial flow calculations. *International Journal for Numerical Methods in Fluids* 1997; **24**:671–691.
22. Youngs DL. Time-dependent multi-material flow with large fluid distortion. In *Numerical Methods for Fluid Dynamics*, Morton KW, Baines MJ (eds). Academic: New York, 1982; 273–285.
23. Udaykumar HS, Kan HC, Shyy W, Tran-Son-Tay R. Multiphase dynamics in arbitrary geometries on fixed Cartesian grids. *Journal of Computational Physics* 1997; **137**:366–405.
24. Chorin AJ. Numerical solution of the Navier–Stokes equations. *Mathematics of Computation* 1968; **22**(104): 745–762.
25. Ye T, Mittal R, Udaykumar HS, Shyy W. An accurate Cartesian grid method for viscous incompressible flows with complex immersed boundaries. *Journal of Computational Physics* 1999; **156**:209–240.
26. Peskin CS. Numerical analysis of blood flow in the heart. *Journal of Computational Physics* 1977; **25**: 220–252.
27. Udaykumar HS, Kan H-C, Shyy W, Tran-Son-Tay R. Multiphase dynamics in arbitrary geometries on fixed Cartesian grids. *Journal of Computational Physics* 1997; **137**:366–405.
28. Kan H-C, Udaykumar HS, Shyy W, Tran-Son-Tay R. Hydrodynamics of a compound drop with application to Leukocyte modelling. *Physics of Fluids* 1998; **10**:760–774.
29. Brackbill JU, Kothe DB, Zemach C. A continuum method for modelling surface tension. *Journal of Computational Physics* 1992; **100**:335–354.
30. Lafaurie B, Nardone C, Scardovelli R, Zaleski S, Zanetti G. Modelling merging and fragmentation in multiphase flows with SURFER. *Journal of Computational Physics* 1994; **113**:134–147.
31. Williams MW, Kothe DB, Puckett EG. Accuracy and convergence of continuum surface-tension models. In *Fluid Dynamics at Interfaces*, Shyy W, Narayanan R (eds.). Cambridge University Press: Cambridge, 1999; 295–305.
32. Meier M, Yadigaroglu G, Smith BL. A novel technique for including surface tension in PLIC-VOF methods. *European Journal of Mechanics B/Fluids* 2002; **21**:61–73.
33. Harmathy TZ. Velocity of large drops and bubbles in media of infinite or restricted extent. *A.I.Ch.E. Journal* 1960; **6**:281–288.
34. Clift R, Grace JR, Weber ME. *Bubbles, Drops and Particles*. Academic Press: New York, 1978.

